



**HAL**  
open science

## Two-step sintering of alumina nano-powders: A discrete element study

Brayan Paredes-Goyes, Aatreya Manjulagiri Venkatesh, David Jauffrès,  
Christophe L. Martin

### ► To cite this version:

Brayan Paredes-Goyes, Aatreya Manjulagiri Venkatesh, David Jauffrès, Christophe L. Martin. Two-step sintering of alumina nano-powders: A discrete element study. *Journal of the European Ceramic Society*, 2023, 43 (2), pp.501-509. 10.1016/j.jeurceramsoc.2022.10.001 . hal-03904166v1

**HAL Id: hal-03904166**

**<https://hal.science/hal-03904166v1>**

Submitted on 16 Dec 2022 (v1), last revised 29 Sep 2023 (v2)

**HAL** is a multi-disciplinary open access archive for the deposit and dissemination of scientific research documents, whether they are published or not. The documents may come from teaching and research institutions in France or abroad, or from public or private research centers.

L'archive ouverte pluridisciplinaire **HAL**, est destinée au dépôt et à la diffusion de documents scientifiques de niveau recherche, publiés ou non, émanant des établissements d'enseignement et de recherche français ou étrangers, des laboratoires publics ou privés.

# Two-step sintering of alumina nano-powders: A discrete element study

Brayan Paredes-Goyes<sup>a</sup>, Aatreya Manjulagiri Venkatesh<sup>a</sup>, David Jauffres<sup>a</sup>,  
Christophe L. Martin<sup>a</sup>

<sup>a</sup>*Univ. Grenoble Alpes, CNRS, Grenoble INP, SIMaP, F-38000 Grenoble, France*

---

## Abstract

Avoiding grain growth during sintering of ceramic nano-powders is of great technological interest. Although two-step sintering is an effective technique to achieve this goal, the mechanisms at play are not well understood. This study adapts our previous discrete model to investigate the conventional and two-step sintering of large nano-powder packings. The densification and grain growth results agree qualitatively well with experimental data on alumina. Simulations confirm that faster heating rates retard grain growth in conventional sintering of nano-alumina. Our results support the hypothesis that the success of nano-alumina two-step sintering relies on the sharp increase in the activation energy of the grain boundary mobility at low temperatures. Simulations indicate a transition temperature of 1100°C and that at least a 2.5-fold increase in activation energy is required to explain the suppression of grain growth. The relative weights of surface diffusion and of grain boundary motion for grain growth are clarified.

*Keywords:* nano-powders, two-step sintering, grain growth, alumina, discrete element method

---

## 1. Introduction

Solid-state sintering produces dense or density-controlled materials from ceramic or metallic powders using thermal energy. The driving force for sintering is the reduction in the total interfacial energy of the system [1, 2]. There are two contributions to the reduction of the product  $\gamma A$ , where  $\gamma$  is the average interface energy and  $A$  is the total interface area of the system:  $A d\gamma$  and  $\gamma dA$ . Thus, during sintering, a coupling between two mechanisms occurs: densification that reduces interfacial energy ( $d\gamma$ ) by replacing solid-gaz interfaces by less energetic solid-solid interfaces, and coarsening that reduces interfacial area ( $dA$ ) [1, 3]. In general, materials scientists and practitioners favor densification while attempting to limit coarsening.

This is especially true when starting from nano-powders (typically  $< 100$  nm grain size) that have great scientific and technological interest. The short diffusion distances in nano-powders inherently favor both grain growth and densification kinetics. For nano-powders, keeping submicronic size grains while ensuring a nearly dense material is challenging. A fast heating rate is an efficient processing method to enhance densification over grain-growth. It is based on the usual condition for most materials that activation energies of grain boundary diffusion along the boundary (densification) are higher than that of grain boundary diffusion perpendicular to the boundary (grain growth) [2]. Fast heating rates may be effectively combined with a modification of the thermal cycle, using a combination of high and low temperatures. This so-called two-step sintering technique may be declined in several variants [4]. Following the two-step approach proposed by Chen and Wang on  $Y_2O_3$  [5], Yang et al. [6, 7] have recently demonstrated the effectiveness of

26 two-step sintering technique to densify  $\text{Al}_2\text{O}_3$  ceramic nano-powders while  
27 keeping small grain size ( $\approx 40$  nm).

28 The reason for the suppression of grain growth in the two-step sintering  
29 process is not clarified yet. The interplay between surface diffusion, grain  
30 boundary diffusion along and perpendicular to the grain boundary is not  
31 sufficiently documented to unambiguously propose a clear scenario. This  
32 task is made more difficult by the fact that, in conjunction with temperature  
33 changes, the microstructure itself undergoes profound alterations. The initial  
34 material is granular and begins as an assembly of discrete particles that  
35 interact with small contacts. It ends as a set of grains with small isolated  
36 pores remaining.

37 Numerical modeling can provide a better understanding of the grain  
38 growth of nano-powders during conventional and two-step sintering. At the  
39 atomistic scale using molecular dynamics, Ding et al. [8] provided insights  
40 into the mechanisms of neck and grain growth during the sintering of 2 and  
41 3 nanoparticles. Depending on the crystalline orientation of the grains, they  
42 observed the disappearance of the grain boundary and the switch of neck  
43 growth mechanisms halfway during the sintering process. At the particle  
44 scale, Benabou and Wang [9] used the surface evolver approach to simulate  
45 the sintering of up to 40 particles. The detailed description of the surfaces  
46 allowed them to observe the elimination of pores and the disappearance of  
47 small particles by grain growth. Monte Carlo methods can also model effi-  
48 ciently the sintering of a reasonable number of initial particles with realistic  
49 interactions [10]. There is a drastic decrease in particle number with coarsen-  
50 ing. Thus, a representative packing with a large initial number of particles is

51 needed to properly study the microstructure evolution in simulations. Using  
52 discrete element modeling (DEM), we have already successfully investigated  
53 grain growth occurring during the sintering of large packings of micronic  
54 alumina particles (up to 400 000) [11].

55 The aim of this study is to extend our previous work to analyze grain  
56 growth and densification of nano-sized alumina during conventional and two-  
57 step sintering. Section 2 summarizes our model with some modifications to  
58 correctly model nano-powders. The simulations and comparison with ex-  
59 perimental data of conventional sintering are presented in Section 3. These  
60 simulations are performed for different heating rates. The evolution of den-  
61 sity, densification rate and grain size with temperature are reported and  
62 critically compared to experimental data from Yang et al. [6]. The volumes  
63 transferred by surface diffusion and grain boundary migration are quantified.  
64 Section 4 presents two-step sintering simulations, their comparison to exper-  
65 imental data and a discussion on the origin of the absence of grain growth.

## 66 **2. Model description**

67 The details of the model (contact laws, contact size, grain growth model)  
68 can be found in [11]. Here we summarize its main ingredients and report  
69 the material parameters used in the simulations. In DEM, particles are rep-  
70 resented as spheres that are progressively truncated at contacts with other  
71 particles as sintering proceeds. The powder compact is modeled as a 3D  
72 random assembly of spherical particles interacting through their contacts.  
73 At each time step, all contacts are considered and contact forces are calcu-  
74 lated and summed up for all particles. Particle velocities and new positions

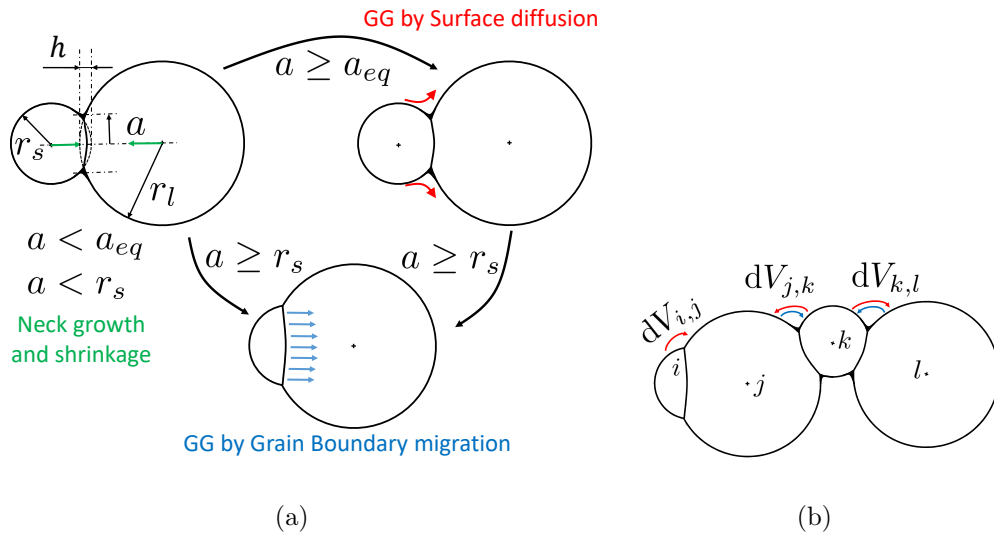


Figure 1: Graphical summary of the model. (a) Grain growth (GG) by Surface diffusion is activated after neck growth reaches the equilibrium configuration. Grain growth by Grain Boundary migration can be attained after GG by surface diffusion or directly after neck growth. (b) Volume exchange  $dV$  is always from small to large particle when the small particle has only one contact  $(i, j)$ . For small particles with more than one contact  $((j, k)$  and  $(k, l))$ , a large particle may give volume  $dV$  to a small one with probability  $P_{s,l}$ .

75 are updated using a velocity-Verlet algorithm. As proposed in our earlier  
76 work [12] and classically adopted by other researchers in DEM simulations  
77 of sintering [13, 14, 15, 16, 17, 18], normal contact forces appear between  
78 particles including two components. The viscous component introduces the  
79 diffusion coefficient along the grain boundary  $D_{GB} = D_{0GB} \exp \frac{-Q_{GB}}{RT}$  with  
80 temperature dependence (activation energy  $Q_{GB}$ ). This component opposes  
81 the relative motion between the two particles. The tensile component (also  
82 known as the sintering force) introduces the surface energy  $\gamma_S$ . The expres-  
83 sion of the normal force is derived from results obtained by Bouvard et al.  
84 [19] and Pan et al. [20] and accounts for sintering by coupled grain boundary  
85 diffusion and surface diffusion, typical of solid state sintering of oxide ceram-  
86 ics. The contact radius  $a$  is calculated here from the model of Pan et al. [20]  
87 for particles of different sizes. The size of the contact plays an important role  
88 in the model as it dictates the transition from one mechanism to another.  
89 The equilibrium contact radius  $a_{eq}$ , at which the sum of the grain boundary  
90 and surface energies reaches a local minimum, is given by the equilibrium  
91 dihedral angle  $\Psi_{eq}$ . When the contact size becomes larger than  $a_{eq}$ , grain  
92 growth (GG) by surface diffusion becomes active, unless the smallest parti-  
93 cle is itself smaller than the contact, in which case GG by grain boundary  
94 migration becomes active (Fig. 1a).

95 Grain growth is modelled by simply considering that an exchange of mat-  
96 ter  $dV$  results in a radius decrease and a radius increase for the two particles  
97 in contact. The flux of matter  $\frac{dV}{dt}$  originates from two contributions: *Surface*  
98 (*S*) diffusion or *Grain Boundary Migration (GBM)*. The surface diffusion

99 contribution writes:

$$\left(\frac{dV}{dt}\right)_S = -4\pi \frac{\delta_S D_{0S} \exp\left(\frac{-Q_S}{RT}\right) \gamma_S \Omega \frac{1}{r_l + r_s - h} a}{k_B T} \quad a \geq a_{eq} \quad (1)$$

100 where  $h$  is the geometric indentation between the two spherical discrete el-  
 101 ements (Fig. 1a),  $k_B T$  has the usual meaning,  $\Omega$  is the atomic volume and  
 102  $\delta_S$  is the thickness of the diffusion layer. The Grain Boundary Migration  
 103 diffusion contribution writes:

$$\left(\frac{dV}{dt}\right)_{GBM} = -2M_{0GB} \exp\left(\frac{-Q_{GBM}}{RT}\right) \gamma_{GB} \left(\frac{1}{r_l} - \frac{1}{r_s}\right) [\pi a^{*2}] \quad a \geq r_s \quad (2)$$

104 with  $a^*$  the contact radius when Grain Boundary Migration becomes active.  
 105 Both Eqs. (1) and (2) have temperature dependence through Arrhenius law  
 106 with pre-exponential factors  $D_{0S}$  and  $M_{0GB}$ , and activation energies  $Q_S$  and  
 107  $Q_{GBM}$ , respectively. Note that as sketched in Fig. 1a, the two contributions  
 108 are mutually exclusive, i.e. only one (or none) is active at a given point for  
 109 a contact.

110 When Grain Boundary Mobility is active ( $a > r_s$ ), by default the volume  
 111 of matter flows from the small to the large particle. We have observed that  
 112 this simplistic assumption triggers abnormal grain growth in our simulations  
 113 for nano-sized particles. As compared to our previous work in [11], we have  
 114 thus added an ingredient to the model that controls the occurrence of abnor-  
 115 mal grain growth by introducing some departure from this default condition.  
 116 This is carried out by stating that a small particle that has two or more  
 117 contacts (particle  $k$  in Fig. 1b) has a probability  $P_{s,l}$  to have positive matter  
 118 flux from the larger one. This scenario is supported by finite difference simu-  
 119 lations on particles of different sizes for two or three particles in contact [21].  
 120 For nanosized particles, these authors reported the intriguing result that a



121 small particle in contact with two larger ones can develop some resistance to  
122 invasion. In particular, they showed that, rather than shrinking, the small  
123 particle grows at the expense of the two larger ones. Eventually, the small  
124 particle always disappears as the boundary migrates. This result was fur-  
125 ther refined by molecular dynamics simulations of nanoparticles sintering [8]  
126 that showed that many different scenarios could exist, depending mainly on  
127 the initial crystalline misalignment between particles. These results indicate  
128 that local curvature (or grain size for spherical grains) may not always dic-  
129 tate the grain boundary velocity when departing from the simplistic model  
130 of two grains. This is consistent with recent experimental results that reveal  
131 that there is no observed relationship between grain boundary velocity and  
132 curvature in polycrystalline Ni with multiple grain boundaries [22]. These  
133 scenarios cannot be realistically included in DEM simulations with several  
134 hundreds of thousands of particles. The probability  $P_{s,l}$  that a small particle  
135 (with more than one contact) can temporarily eat away a larger one accounts  
136 for these alternative scenarios in a very simple manner. We set this value in  
137 all simulations to  $P_{s,l} = 1/4$ , and observed that this was sufficient to prevent  
138 abnormal grain growth.

### 139 **3. Sintering at constant heating rate**

140 The model described above was applied to simulate the sintering of  $\alpha$ -  
141  $\text{Al}_2\text{O}_3$  nanopowders, which has been thoroughly examined experimentally in  
142 [6, 7]. Starting from a powder cold-compacted to a green density of 0.48,  
143 sintering was carried out at various heating rates. The initial powder (before  
144 compaction) was observed by TEM at approximately 5 nm in size, with a

145 narrow initial grain-size distribution (standard deviation normalized by the  
 146 average grain size = 0.23). Numerical specimens were prepared to reproduce  
 147 this initial green packing. We observed in our simulations that applying a  
 148 500 MPa axial stress on this packing already triggered at room temperature  
 149 some grain coarsening (i.e.  $a \geq a_{eq}$  or  $a \geq r_s$ ) due to surface energy effects.  
 150 This is because adhesive forces induce local elastic strains that are far from  
 151 negligible for nano-powders. Using the DMT model, which is well adapted  
 152 for hard and small particles [23, 24], the equilibrium contact radius  $a$  of two  
 153 identical spheres of radius  $r$  with Young’s modulus  $E$  and Poisson’s ratio  $\nu$   
 154 writes:

$$\frac{a}{r} = \frac{3}{2}\pi \frac{\gamma_s}{r} \frac{1 - \nu^2}{E} \quad (3)$$

155 yielding a value  $a/r \approx 0.17$ . Eq. (3) is derived for two particles without  
 156 external stress. Adding external stress further increases strain at contacts,  
 157 which should lead to irreversible grain deformation and coalescence even  
 158 below 800°C. Thus, we started our sintering simulations with an average  
 159 grain size of 10 nm, which is in good accordance with SEM observations [6].  
 160 Packings made of 400 000 randomly located particles, with an initial relative  
 161 standard deviation of the grain-size distribution of 0.23 were compacted up  
 162 to 0.50 relative density in a periodic simulation box to obtain the starting  
 163 green powder. This large number of initial particles is needed to obtain  
 164 statistically meaningful results at the end of sintering when a large number  
 165 of particles have disappeared (see Appendix A).

166 Material parameters used in the simulations are summarized in Table 1.  
 167 Activation energies for grain boundary diffusion,  $Q_{GB}$ , surface diffusion,  $Q_S$ ,  
 168 and grain boundary mobility,  $Q_{GBM}$ , were taken directly from the literature,

$\delta_{GB}D_{0GB}$ (m <sup>3</sup> /s)	1.04x10 <sup>-11</sup>	$Q_{GB}$ (kJ/mol)	475 [26]
$D_{0S}$ (m <sup>2</sup> /s)	7.2x10 <sup>-05</sup>	$Q_S$ (kJ/mol)	313.8 [27]
$M_{0GB}$ (m <sup>3</sup> /(N.s))	0.02 [28, 11]	$Q_{GBM}$ (kJ/mol)	443 [28]
$\Psi_{eq}$ (°)	138 [29]	$\Omega$ (m <sup>3</sup> )	2.11x10 <sup>-29</sup> [27]
$\gamma_S$ (J/m <sup>2</sup> )	0.905 [27]	$\gamma_{GB}$ (J/m <sup>2</sup> )	2 $\gamma_S \cos(\Psi_{eq}/2)$

Table 1: Material parameters used for alumina.

169 and are the same as those used for micronic alumina powder sintering in [11].  
170 The prefactor of the grain boundary diffusion coefficient was adjusted to fit  
171 the experimentally observed relative density at  $T_1 = 1150^\circ\text{C}$  for a  $10^\circ\text{C}/\text{min}$   
172 heating rate. The partially sintered packing obtained at this temperature  
173 is used for two-step sintering simulations in section 4. The prefactor of the  
174 surface diffusion coefficient was chosen to keep the same ratio of the grain  
175 boundary diffusion to surface diffusion ( $\xi = 0.001$ ) as in our previous work  
176 for a temperature of  $1350^\circ\text{C}$ . For small values of  $\xi$  (associated with the  
177 lower temperatures simulated here), the work of Bouvard and McMeeking  
178 [25] suggests that the tensile term in the normal force expression depends  
179 only weakly on  $\xi$ . This ensures that the parameters of the sintering model  
180 used for micronic sizes remain valid [11]. Note that the activation energies  
181 in Table 1 are consistent with the range proposed in [6] for nano-powders.

182

183 Fig. 2 shows the evolution of the densification rate  $d\rho/dt$  for the three  
184 simulated heating rates (3, 5 and  $10^\circ\text{C}/\text{min}$ ). Fig. 2 indicates that, owing  
185 to the very small size of the starting powders, densification is already active  
186 at  $800^\circ\text{C}$ . This may be understood by recognizing that the sintering force

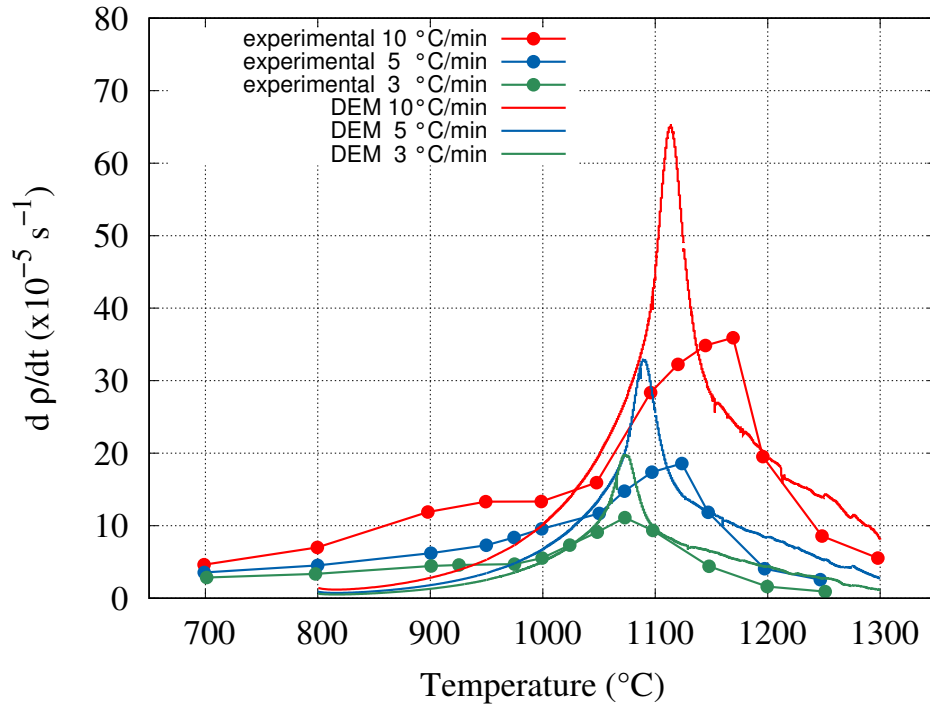


Figure 2: Densification rate evolution with temperature for three heating rates: 3, 5 and 10 °C/min. Experimental data is from [6]

187 expression in our model leads to a time normalization (before coarsening  
 188 mechanisms start to play a role) that scales with the mean particle size,  $G$   
 189 to the power 4:  $\tau \propto \langle r \rangle^4$ . This is in line with classic analytical models that  
 190 lead to densification rates scaling with  $G^4$  [30].

191 While our simulations indicated that the heating rate has a minor in-  
 192 fluence on the sintering of micro-alumina [11], this is no more the case for  
 193 nano-alumina. For all three heating rates, the densification rate increases  
 194 to a maximum and decreases to very small values when full density is ap-  
 195 proached. The temperature at which this maximum occurs increases with

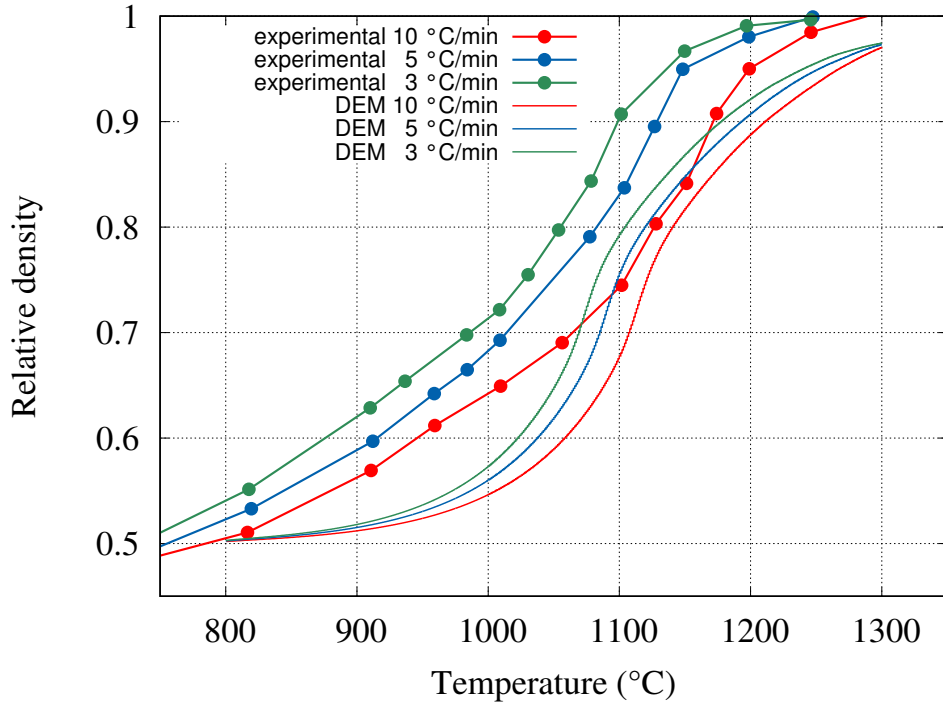


Figure 3: Relative density evolution with temperature for three heating rates: 3, 5 and 10 °C/min. Experimental data is from [6]

196 increasing heating rates. A higher heating rate is associated to a higher maximum  
 197 densification rate: the peak densification rate at 10 °C/min is three  
 198 times as fast as that at 3 °C/min. This is the result of two effects. First,  
 199 Fig. 3 shows the evolution of density with temperature. It indicates that at  
 200 a given temperature, a faster heating rate results in a lower relative density,  
 201 thus keeping the driving force for densification higher. Second, Fig. 4 shows  
 202 that grain growth arises at higher temperatures as the heating rate increases.  
 203 The occurrence of the maximum densification rate is well correlated in all  
 204 three simulations to the initiation of grain growth. Fig. 4 indicates that the

205 heating rate has a clear effect on the final grain size.

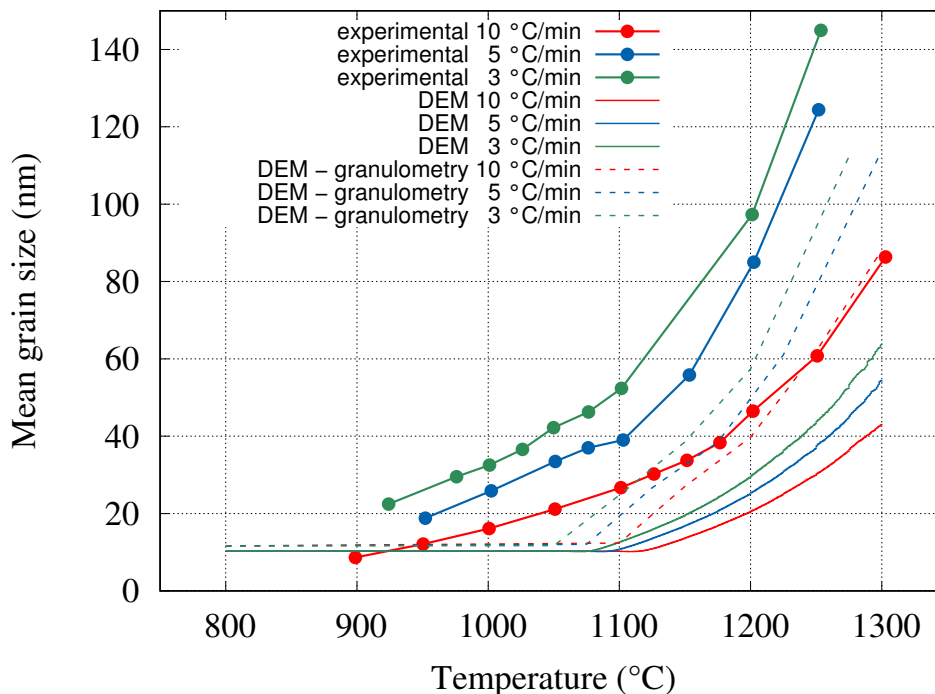


Figure 4: Mean grain size evolution with temperature for three heating rates: 3, 5 and 10 °C/min. Experimental data is from [6]. The dashed lines represent the mean grain size of the DEM packings calculated by image analysis (granulometry algorithm).

206 Figs. 2, 3 and 4 include experimental data from [6] for comparison. Recall  
 207 that the only material parameter that was adjusted was the prefactor of the  
 208 grain boundary diffusion coefficient to fit approximately the experimental  
 209 relative density for 10 °C/min at  $T_1 = 1150^\circ\text{C}$ . The comparison demon-  
 210 strates that the DEM simulations are able to capture qualitatively well all  
 211 relevant experimental features. In particular, the bell shape of the densifi-  
 212 cation rate with temperature (Fig. 2), the S shape of the evolution of the  
 213 density with temperature (Fig. 3), and the concave shape of the grain growth

214 (Fig. 4). However, some quantitative differences are clear. In particular, the  
215 DEM simulations underestimate the initial sintering activity of the powder at  
216 low temperature (both densification rate and grain growth). Because of the  
217 strong model assumptions, it was not possible to fit the densification curves  
218 at both low and high temperatures. The choice was made to fit densities  
219 at high temperatures and consequently the densification is underestimated  
220 at low temperatures. For grain growth, the delayed initiation is linked to  
221 our simplistic assumption that surface diffusion and grain boundary motion  
222 are mutually exclusive and abruptly starts only when the contact radius is  
223 above a critical radius (Fig. 1). This results in DEM relative density curves  
224 lagging behind the experimental curves at low temperature. In addition, we  
225 observed that the mean grain size of DEM packings calculated using image  
226 analysis on 3D images generated from the simulations (dashed lines in Fig.  
227 4) results in larger grain size that are in better accordance with experimental  
228 data. This methodology, comparable to the one used by [6], is detailed in  
229 Appendix B.

230 Keeping in mind these discrepancies with experimental data, the mecha-  
231 nisms that lead to grain growth in nano-powders can still be analysed using  
232 the detailed results of DEM simulations. Fig. 5a shows on a log-scale the  
233 mean volume transferred per contact at a given temperature. It is separated  
234 into the two contributions given by Eqs. (1) and (2). Fig. 5a indicates that  
235 at low temperature, surface diffusion is the main contributor to grain growth,  
236 although this contribution becomes significant only above 1070-1100 °C, de-  
237 pending on the heating rate. This is in line with the general view that at  
238 lower sintering temperatures, surface diffusion dominates matter redistribu-

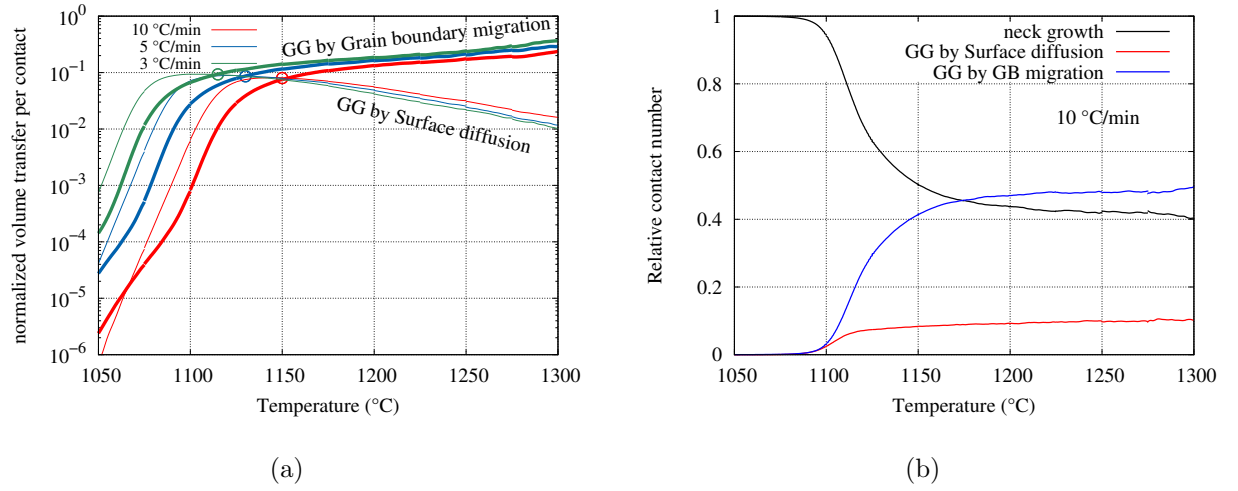


Figure 5: a) Evolution of the mean volume transferred per contact (normalized by the mean volume of particles) with temperature for three heating rates: 3, 5 and 10  $^{\circ}\text{C}/\text{min}$ . Two contributions for grain growth (GG) are shown: surface diffusion (Eq. (1)) and grain boundary migration (Eq. (2)). Circles indicate the temperature at which grain boundary migration contribution exceeds surface diffusion contribution. b) Evolution of the relative contact number (normalized by the total number of contacts) for each possible status: neck growth, GG by surface diffusion and GB migration for 10  $^{\circ}\text{C}/\text{min}$ .



239 tion during grain growth. Grain boundary migration becomes dominant at  
240 higher temperature with large transfer of volumes from one particle to an-  
241 other (compared to the actual volume of particles). Fig. 5b confirms this  
242 result. It shows the evolution of contact status as temperature increases for  
243 the 10 °C/min heating rate (it is representative of all 3 heating rates). At low  
244 temperatures, all contacts are in the initial neck growth status and gradually  
245 shift to grain growth by surface diffusion and by grain boundary migration.  
246 Note that below 1100 °C, Fig. 5b shows that very few contacts contribute  
247 to grain growth, thus explaining the very small volume transfer indicated by  
248 Fig. 5a for these temperatures at 10 °C/min.

249 Because new contacts arise between particles all along sintering due to  
250 densification and rearrangement of particles, neck growth and shrinkage are  
251 still active leading to the continuation of densification. These results are sim-  
252 ilar qualitatively to those obtained for micronic powders [11]. It shows that  
253 conventional sintering models can be applied to nano-powders and reproduce  
254 their very good sinterability and significant grain growth.

255 Fig. 5a also explains the results shown in Fig. 4 which indicate the  
256 beneficial effect of higher heating rates to retard grain-growth. The shift from  
257 surface diffusion to grain boundary migration triggers significant grain growth  
258 in our model. This shift arises at higher temperature for faster heating rates.  
259 We believe that our model underestimates grain growth by surface diffusion  
260 at low temperature (as proved by the grain size curves lagging behind the  
261 experimental curves at low temperature, Fig. 4). Still, Fig. 5a points to  
262 an interesting lever to retard grain-growth: delaying the migration of grain  
263 boundaries, which is much more effective than surface diffusion for grain

	$\rho_c$	$G$ (nm)	$T_1$ ( $^{\circ}\text{C}$ )	$T_2$ ( $^{\circ}\text{C}$ )
10 $^{\circ}\text{C}/\text{min}$	0.82	13.6	1150	1025
5 $^{\circ}\text{C}/\text{min}$	0.76	10.7	1100	975
3 $^{\circ}\text{C}/\text{min}$	0.72	10.2	1075	950

Table 2: Main parameters of the second-step sintering.  $\rho$ ,  $G$  : density and mean grain size attained in the first step.  $T_1$ : temperature at which this density was obtained, and  $T_2$ : temperature of the second isothermal sintering step.

264 growth.

265 A practical alternative to retard the migration of grain boundaries is  
 266 to actually freeze this mechanism by using two-step sintering, which takes  
 267 advantage of low temperatures in a second prolonged isothermal stage [4].  
 268 This is studied in the next section.

#### 269 4. Two-step sintering

270 Numerical samples originating from constant heating rate simulations  
 271 were retrieved for a second sintering step at a lower constant temperature.  
 272 In line with the experimental procedure adopted in [6], table 2 lists the main  
 273 parameters of these simulations. The densities obtained in simulation at the  
 274 end of the first step ( $\rho_c$ ) are lower than the experimental densities (Fig. 3).  
 275 As input for the second step, we opted to use the microstructure obtained at  
 276 the experimental temperature  $T_1$  instead of the microstructure obtained at  
 277 the same density of experiments.

278

279 First, we ran the simulations of the second step (lower temperature) with

280 the same activation energies as in the first step (higher temperature). In  
281 that case, considerable grain growth is observed. However, Gottstein et al.  
282 [31] observed that at low temperatures the motion of the grain boundary is  
283 controlled by the 3-grains junction lines that have a higher mobility activation  
284 energy. This was the principle employed by Chen and Wang [5] to propose  
285 for the first time the variant of two-step sintering used in the present study.  
286 The effect of the junction mobility results in a higher apparent activation  
287 energy of the grain boundary motion below a transition temperature. This  
288 has been measured experimentally for aluminum crystals [32], tungsten [33]  
289 and yttria-stabilized zirconia [34]. The multiplicative factor of the observed  
290 increase in activation energy is between 1.9 and 2.6. Yang et al. [6] suggested  
291 that this activation energy increase could also occur in the case of alumina.  
292 Thus, we have tested a higher activation energy of grain boundary migration  
293  $Q_{GBM}$  for low temperatures in our simulations.

294 Fig. 6 shows the grain boundary mobility as a function of temperature,  
295 where the slope represents the value of the activation energy  $Q_{GBM}$ . Data  
296 points are collected from the literature [28, 35, 36, 37, 38, 39]. For the first  
297 step, we choose  $Q_{GBM}=443\text{kJ/mol}$  according to alumina experimental data  
298 at high temperatures (red line). To the best of our knowledge, no activation  
299 energies for junction mobility or for grain boundary mobility at temperatures  
300 below  $1325^\circ\text{C}$  are reported in the literature. Based on the data for other  
301 materials commented above, we choose an activation energy  $2.5\times Q_{GBM}$  (blue  
302 line) for the second step. Regarding the transition temperature, there is also  
303 no experimental data for alumina. Based on our simulation results of grain  
304 size (Fig. 4), we choose  $T = 1100^\circ\text{C}$  as below this temperature grain growth

305 is negligible. Simulations indicate that using lower transition temperatures,  
 306 very high nonphysical values of activation energy ( $> 3 \times Q_{GBM}$ ) would be  
 307 needed to suppress grain growth. We corroborated that using the selected  
 308 activation energy and transition temperature in the second step has negligible  
 309 effects in the results of the first step.

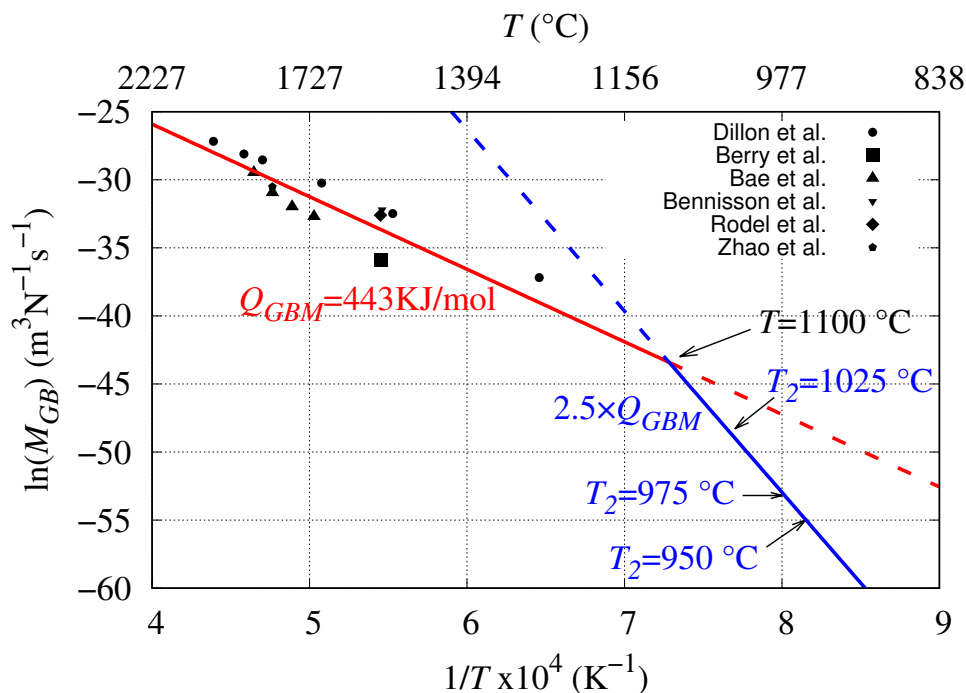


Figure 6: Grain boundary mobility of alumina with data points from the literature [28, 35, 36, 37, 38, 39].  $Q_{GBM}=443\text{KJ/mol}$  (red line) is the standard value used for the first step. An increase of  $2.5 \times Q_{GBM}$  (blue line) is considered for the second step with a transition temperature at  $T = 1100^\circ\text{C}$ .  $T_2$  is the temperature of the second step according to table 2.

310 Simulations of the second step were carried out for the three heating  
 311 rates studied in the previous section, using  $2.5 \times Q_{GBM}$  at low temperatures.  
 312 Fig. 7 illustrates the 3D microstructural evolution from DEM simulations

313 for conventional and two-step sintering for the heating rate  $5^\circ\text{C}/\text{min}$ . From  
314 0.50 to 0.76 relative density ( $T = 800^\circ\text{C} \rightarrow T_1 = 1100^\circ\text{C}$ ), the number of  
315 particles decreases (from 400 000 to 263 000) due to some volume transfer but  
316 without significant increase of the mean grain size. Conventional sintering  
317 ( $T_1 = 1100^\circ\text{C} \rightarrow T = 1175^\circ\text{C}$ ) leads to grain growth as already indicated in  
318 Fig. 4 with a further decrease in particle number (from 263 000 to 36 000). In  
319 contrast, two-step sintering ( $T_2 = 975^\circ\text{C}$ ) keeps the same number of particles  
320 and mean grain size.

321 Fig. 8 shows the grain size-density trajectories obtained by simulations  
322 for both conventional sintering and in two steps. The simulations of two-step  
323 sintering were able to reproduce the experimental results, i.e. annihilating  
324 the grain growth while continuing densification. During the second step a  
325 slight grain growth is observed at  $10^\circ\text{C}/\text{min}$ , while no grain growth occurs  
326 for the two slower heating rates. This is due to a combined effect of much  
327 higher grain boundary mobility for  $10^\circ\text{C}/\text{min}$  (higher  $T_2$ , table 2 and Fig. 6)  
328 and a more advanced state of the microstructure on the sintering trajectory  
329 at the beginning of the second step in our simulations, which favors grain  
330 growth.

331 In order to inspect the alterations produced by two-step sintering on  
332 grain growth, Fig. 9 shows the volume transferred by surface diffusion and  
333 grain boundary motion for one and two-step sintering. In accordance with  
334 Fig. 8, the grain growth from both mechanisms is lower in two-step than  
335 in conventional sintering. The decrease of the volume transferred by surface  
336 diffusion is essentially due to the lower temperature employed in two-step  
337 sintering. One way to further decrease it is to use a powder with a narrow

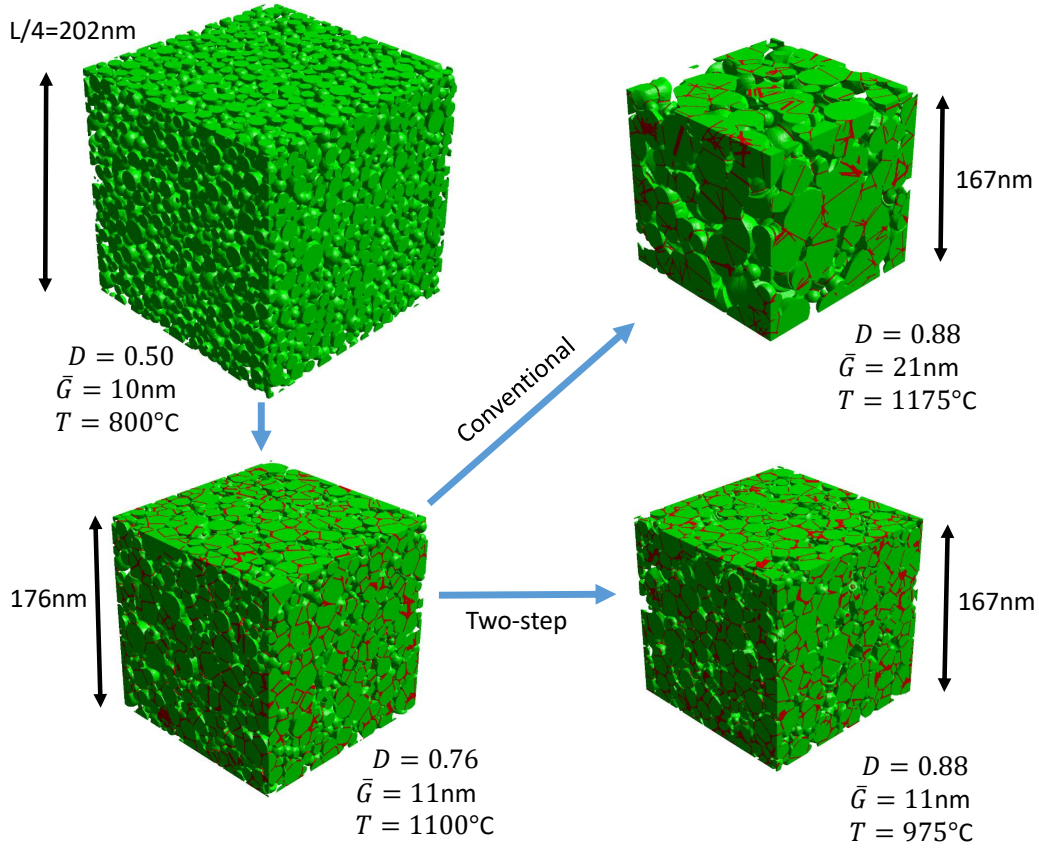


Figure 7: Evolution of DEM microstructures at  $5^{\circ}\text{C}/\text{min}$  heating rate . The sintered necks are represented by two inverted tori tangent to each particle [11]. Grain boundaries are shown in red. Only a portion of the total simulation cube ( $L^3$ ) is shown for clarity.

338 initial size distribution as indicated for nanopowders by Fang et al. [40]  
 339 and verified by simulations in micro-alumina in our previous work [11]. The  
 340 decrease of volume transmitted by grain boundary migration is much more  
 341 substantial (Fig. 9) and caused both by the reduction of process temperature  
 342 and, mainly, by the increase of the associated activation energy (Fig. 6).

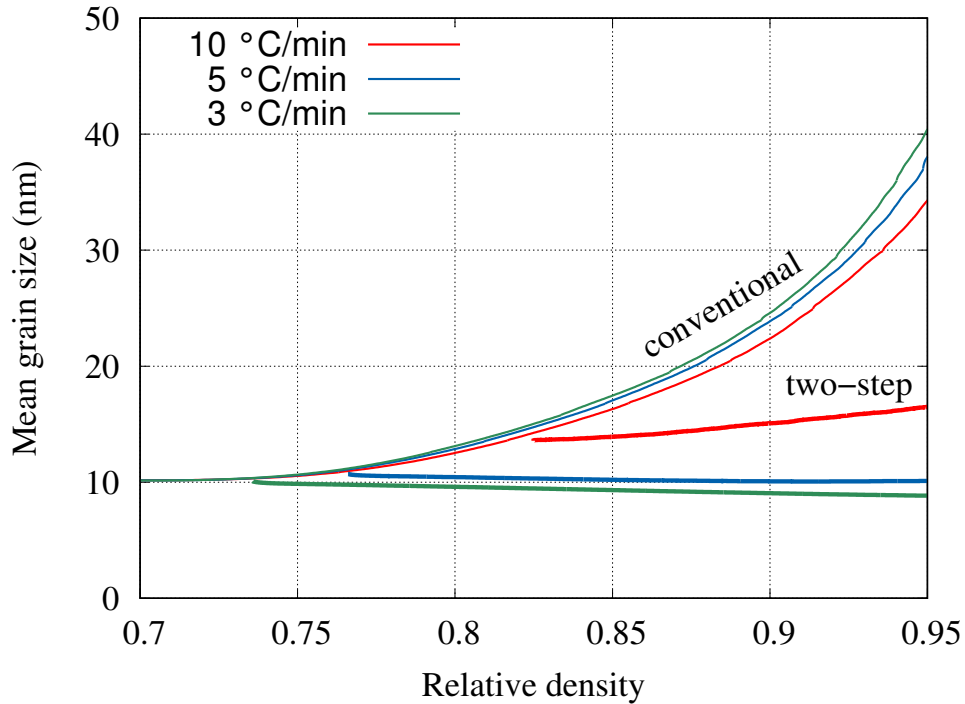


Figure 8: Grain size - density trajectories for three heating rates: 3, 5 and 10 °C/min obtained by DEM simulations. Two-step sintering curves are represented by thicker lines, while thinner lines represent conventional sintering. The second step is performed at constant temperature after a first heating ramp stage. Sintering temperatures are given in Table 2. A high activation energy for grain boundary mobility ( $2.5 \times Q_{GBM}$ ) is used in the second step as sketched in Fig. 6.

343 Therefore, our simulations suggest the validity of the hypothesis proposed  
 344 by Yang et al. [6] on the grain boundary mobility transition as a cause  
 345 for the effectiveness of the alumina two-step sintering. This applies since  
 346 the activation energy of the alumina grain boundary diffusion, that governs  
 347 densification, is assumed constant and is lower than the activation energy  
 348 of GB mobility. We studied the effect of different values of the activation

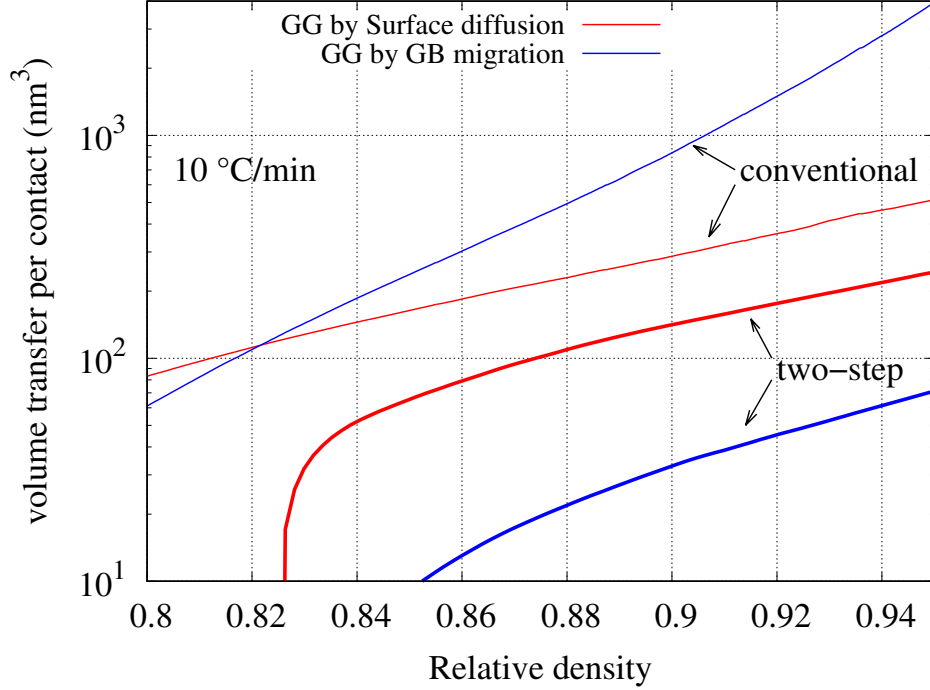


Figure 9: Transferred volume per contact for the two grain growth mechanisms considered in the DEM simulations. Comparison between conventional and two-step sintering.

349 energy of the GB mobility (Fig. 10). Simulations confirm that an increase of  
 350 at least  $2.5 \times Q_{GBM}$  is necessary to suppress grain growth. We also observed  
 351 that keeping the same value for the activation energy ( $1.0 \times Q_{GBM}$ , pink  
 352 curve), the two-step trajectory actually accelerates grain growth as compared  
 353 to conventional sintering for 10 °C/min (dashed red line). This is again  
 354 due to the fact that the activation energy of the grain boundary mobility is  
 355 lower than that of the grain boundary diffusion. The sintering temperature  
 356 being low ( $T_2 = 1025$  °C), a significant grain growth is obtained after a long  
 357 sintering time (170h), which is contradictory to experimental data for two-



358 step sintering. The densification kinetics is very slow in this case, due to  
 359 the significant growth of grains. For two-step sintering and  $2.5 \times Q_{GBM}$ , the  
 360 times indicated (in hour) in Fig. 10 are in line with experimental data, which  
 361 report full densification after 40 hours of sintering in the second step [6].

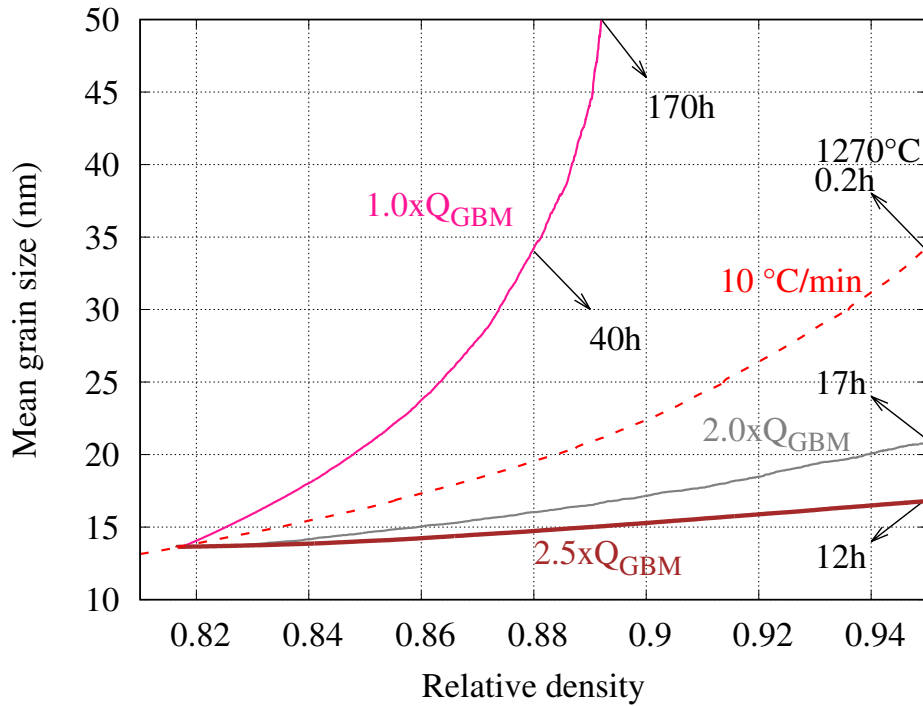


Figure 10: Grain size-density trajectories for different  $Q_{GBM}$  in the second step at  $T_2 = 1025 \text{ }^\circ\text{C}$  (solid lines) and in conventional sintering for  $10 \text{ }^\circ\text{C/min}$  (dashed line). Times in hour are indicated to illustrate the associated sintering kinetics.

## 362 5. Conclusion

363 The sintering behaviour, even for only two nanoparticles, can be com-  
 364 plex and strongly dependant on the crystalline orientation as shown in [8].

365 Our discrete model at the particle scale cannot reproduce all the subtleties  
366 that can be simulated at the atomic scales. Still, our simulations show good  
367 agreement with experimental data in terms of the evolution of the densifica-  
368 tion rate, density and grain size. However, the very early densification and  
369 grain growth of nano-powders reported by Yang et al. [6] are not correctly  
370 reproduced by the model.

371 A limitation in our discrete modeling is the assumption of spherical par-  
372 ticles that indent during sintering. This hypothesis is particularly challenged  
373 in the last stage of grain growth where a typical pear shape has been sug-  
374 gested by two-particles modeling [20, 41]. Freeing from this assumption,  
375 while keeping the discrete framework, can only be achieved by introducing a  
376 new paradigm such as using level-set representation of particles [42].

377 We observed that for nanoparticles, abnormal grain growth is triggered in  
378 our simulations if we enforce the simplistic rule that small particles are always  
379 eaten away by larger ones. This phenomenon needs further investigation to  
380 clarify the conditions that lead to abnormal grain growth. In particular,  
381 molecular dynamics simulations could help (if they are able to model several  
382 tens of nanoparticles for large physical times) to detect the conditions that  
383 lead to abnormal versus normal grain growth. The transfer of matter from  
384 one grain to another is dictated by the local curvature. For spherical grains,  
385 as used here, the local curvature is uniquely related to particle sizes. This  
386 is clearly simplistic and simulating non-spherical geometries would certainly  
387 provide more realistic information about abnormal grain-growth.

388 With the ability to study thermal cycles during sintering, the model con-  
389 firms the effectiveness of using fast heating rates to retard grain growth in

390 conventional sintering of nano-powders. The mechanisms underlying the effi-  
391 ciency of two-step sintering of alumina and more generally of ceramic oxides  
392 still need some further investigation, both from experiments and modelling.  
393 Still, this study plausibly supports the hypothesis of [6] that a transition of  
394 the apparent activation energy of the grain boundary mobility is the main  
395 reason. Our results suggest that the halting of grain growth in the second  
396 step is explained by a large increase ( $\geq 2.5$ ) of the activation energy of grain  
397 boundary mobility for a transition temperature of 1100° C. Further exper-  
398 imental and numerical studies are needed to confirm these values and to  
399 clarify whether the cause of the mobility activation energy is the junction  
400 drag or some other property of the alumina grain boundary.

401

402 Funding: This project has received funding from the European Union’s  
403 Horizon 2020 research and innovation programme under the Marie Skłodowska-  
404 Curie grant agreement MATHEGRAM No 813202.

## 405 **Appendix A. Influence of the initial packing particle number**

406 DEM has the ability to handle packings with a large number of particles in  
407 a feasible time. Nevertheless, even if millions of particles are considered, this  
408 value is much lower than the number of particles used in experiments. It is  
409 thus necessary to choose a number of particles that lead to a representative  
410 behavior of the real experimental packing. The simulation results should  
411 converge when increasing the number of particles. This is more critical in  
412 simulations of grain growth as the number of particles decreases significantly

413 during sintering. Fig. A.1 shows the evolution of the mean grain size with  
 414 temperature for packings with initially: 4 000, 40 000 and 400 000 particles.  
 415 Below 1200°C, all three packings have the same behaviour. As the number  
 416 of particles continues to decrease, some discrepancies appear for the two  
 417 smaller packings. This is critical at the end of sintering for the 4 000 packing,  
 418 as very few particles remain (only 12 at 1300 °C). We note that results  
 419 converge to the 400 000 packing curve, thus this initial packing is used for all  
 420 simulations. For a parallel simulation on four CPU cores, the computational  
 421 time is approximately five days.

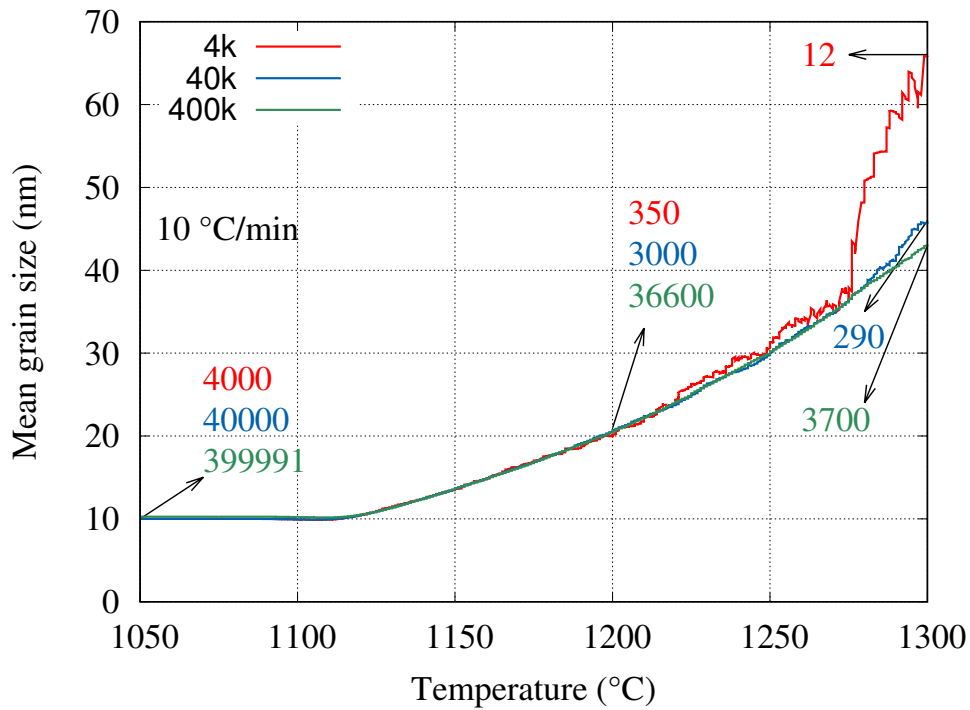


Figure A.1: Evolution of the mean grain size with temperature for increasing number of particles in the initial packing (4 000, 40 000 and 400 000). The number of particles remaining for each packing is indicated at 1050, 1200 and 1300 °C.

## 422 **Appendix B. Calculation of the mean grain size**

423 The simplest method to compute the mean grain size in our DEM simu-  
424 lations is to perform the average of the diameter over all particles, which are  
425 considered as perfect spheres (with the indented volume kept in the calcula-  
426 tion to account for material deposition at the neck). In experiments, starting  
427 from microstructural observations, significantly different approaches are used  
428 to deal with real non-spherical shapes. To illustrate this, the DEM packings  
429 (indented spheres inverted with torus necks shape [43]) are rendered in 3D  
430 and exported in the form of RAW image stacks (see Fig. 7). To estimate  
431 the mean grain size, we use the granulometric analysis method [44], a widely  
432 used approach in image processing to estimate the size of structural features.  
433 This image analysis is computationally feasible if the number of particles in  
434 the images is around a few thousands. For this purpose, we use packings  
435 with initially 4 000 and 40 000 particles for the initial and intermediate stage  
436 of sintering respectively. In Appendix A, we have shown that the results are  
437 similar to the 400 000 packing at those stages. The granulometry algorithm  
438 in the GrainFind module of GeoDict [45] is then capable of evaluating the  
439 size of grains, first by converting the image stacks into a distance map by  
440 Euclidean distance transform (EDT) and then by fitting pre-defined spheres  
441 into the structure. The spheres are successively fitted into the grain volume  
442 in a descending order, thus giving an estimation of their diameters. In that  
443 sense, it is a purely geometrical measurement as it does not require knowledge  
444 of the characteristics of individual grains and non-spherical complex grains  
445 can be assigned the diameters of the largest spheres that can be inscribed.

446 **References**

- 447 [1] S.-J. L. Kang, *Sintering Densification, Grain Growth,*  
448 *and Microstructure*, Butterworth-Heinemann, Oxford, 2005.  
449 doi:<https://doi.org/10.1016/B978-075066385-4/50000-5>.
- 450 [2] R. K. Bordia, S. J. L. Kang, E. A. Olevsky, Current understanding and  
451 future research directions at the onset of the next century of sintering  
452 science and technology, *Journal of the American Ceramic Society* 100 (6)  
453 (2017) 2314–2352. doi:10.1111/jace.14919.
- 454 [3] G. Bernard-Granger, C. Guizard, New relationships between  
455 relative density and grain size during solid-state sintering of  
456 ceramic powders, *Acta Materialia* 56 (20) (2008) 6273–6282.  
457 doi:10.1016/j.actamat.2008.08.054.
- 458 [4] N. J. Lóh, L. Simão, C. A. Faller, A. De Noni, O. R. Montedo, A review  
459 of two-step sintering for ceramics, *Ceramics International* 42 (11) (2016)  
460 12556–12572. doi:10.1016/j.ceramint.2016.05.065.  
461 URL <http://dx.doi.org/10.1016/j.ceramint.2016.05.065>
- 462 [5] X.-H. Wang, I.-W. Chen, Sintering dense nanocrystalline ceramics with-  
463 out final-stage grain growth, *Nature* 404 (9 March) (2000) 168–171.  
464 URL <https://www.nature.com/articles/35004548>
- 465 [6] H. Yang, L. Li, Y. Li, B. Shen, Y. Kang, L. Zhao, J. Li,  
466 Y. Dong, J. Li, Unveiling exceptional sinterability of ultrafine  $\alpha$ -  
467 Al<sub>2</sub>O<sub>3</sub> nanopowders, *Journal of Materiomics* 7 (4) (2021) 837–844.  
468 doi:10.1016/j.jmat.2020.12.011.

- 469 [7] Y. Dong, H. Yang, L. Zhang, X. Li, D. Ding, X. Wang, J. Li,  
470 J. Li, I. W. Chen, Ultra-Uniform Nanocrystalline Materials via Two-  
471 Step Sintering, *Advanced Functional Materials* 31 (1) (2021) 1–9.  
472 doi:10.1002/adfm.202007750.
- 473 [8] L. Ding, R. L. Davidchack, J. Pan, A molecular dynamics study of  
474 sintering between nanoparticles, *Computational Materials Science* 45 (2)  
475 (2009) 247–256. doi:10.1016/j.commatsci.2008.09.021.  
476 URL <http://dx.doi.org/10.1016/j.commatsci.2008.09.021>
- 477 [9] L. Benabou, X. Wang, Simulation of silver nanoparticles sintering at  
478 high temperatures based on theoretical evaluations of surface and grain  
479 boundary mobilities, *International Journal for Computational Meth-  
480 ods in Engineering Science and Mechanics* 21 (6) (2020) 331–342.  
481 doi:10.1080/15502287.2020.1841334.  
482 URL <https://doi.org/10.1080/15502287.2020.1841334>
- 483 [10] F. Raether, G. Seifert, H. Ziebold, Simulation of Sintering across Scales,  
484 *Adv. Theory Simulations* 2 (7) (2019) 1–19. doi:10.1002/adts.201900048.
- 485 [11] B. Paredes-Goyes, D. Jauffres, J.-M. Missiaen, C. L. Martin, Grain  
486 growth in sintering: a discrete element model on large packings, *Acta  
487 Materialia* 218 (2021) 117182. doi:10.1016/j.actamat.2021.117182.  
488 URL <https://doi.org/10.1016/j.actamat.2021.117182>
- 489 [12] C. L. Martin, L. C. R. Schneider, L. Olmos, D. Bouvard, Discrete el-  
490 element modeling of metallic powder sintering, *Scripta Mater.* 55 (2006)  
491 425–428.

- 492 [13] B. Henrich, A. Wonisch, T. Kraft, M. Moseler, H. Riedel, Simulations of  
493 the influence of rearrangement during sintering, *Acta Materialia* 55 (2)  
494 (2007) 753–762. doi:10.1016/j.actamat.2006.09.005.
- 495 [14] C. Wang, S. H. Chen, The influence of agglomerates on the densification  
496 and microstructural evolution in sintering of a multi-particle system,  
497 *Science China: Physics, Mechanics and Astronomy* 55 (6) (2012) 1051–  
498 1058. doi:10.1007/s11433-012-4743-4.
- 499 [15] S. Nosewicz, J. Rojek, K. Pietrzak, M. Chmielewski, Viscoelastic dis-  
500 crete element model of powder sintering, *Powder Technology* 246 (2013)  
501 157–168. doi:10.1016/j.powtec.2013.05.020.  
502 URL <http://dx.doi.org/10.1016/j.powtec.2013.05.020>
- 503 [16] R. Besler, M. Rossetti Da Silva, J. J. Do Rosario, M. Dosta, S. Heinrich,  
504 R. Janssen, Sintering Simulation of Periodic Macro Porous Alumina,  
505 *Journal of the American Ceramic Society* 98 (11) (2015) 3496–3502.  
506 doi:10.1111/jace.13684.
- 507 [17] H. Xin, W. C. Sun, J. Fish, Discrete element simulations of  
508 powder-bed sintering-based additive manufacturing, *International Jour-  
509 nal of Mechanical Sciences* 149 (November 2017) (2018) 373–392.  
510 doi:10.1016/j.ijmecsci.2017.11.028.  
511 URL <https://doi.org/10.1016/j.ijmecsci.2017.11.028>
- 512 [18] T. Matsuda, Development of a DEM taking account of neck increments  
513 caused by surface diffusion for sintering and application to analysis of the  
514 initial stage of sintering, *Computational Materials Science* 196 (Febru-



- 515 ary) (2021) 110525. doi:10.1016/j.commatsci.2021.110525.  
516 URL <https://doi.org/10.1016/j.commatsci.2021.110525>
- 517 [19] D. Bouvard, R. M. McMeeking, Deformation of Interparticle  
518 Necks by Diffusion-Controlled Creep (1996). doi:10.1111/j.1151-  
519 2916.1996.tb07927.x.
- 520 [20] J. Pan, H. Le, S. Kucherenko, J. A. Yeomans, A model for the sintering  
521 of spherical particles of different sizes by solid state diffusion, *Acta Ma-*  
522 *terialia* 46 (13) (1998) 4671–4690. doi:10.1016/S1359-6454(98)00144-X.
- 523 [21] H. Ch’ng, J. Pan, Sintering of particles of different sizes, *Acta Materialia*  
524 55 (3) (2007) 813–824. doi:10.1016/j.actamat.2006.07.015.  
525 URL <http://linkinghub.elsevier.com/retrieve/pii/S1359645406005337>
- 526 [22] A. Bhattacharya, Y. F. Shen, C. M. Hefferan, S. F. Li, J. Lind, R. M.  
527 Suter, C. E. Krill, G. S. Rohrer, Grain boundary velocity and curvature  
528 are not correlated in Ni polycrystals, *Science* 374 (6564) (2021) 189–193.  
529 doi:10.1126/science.abj3210.
- 530 [23] B. V. Derjaguin, V. M. Muller, Y. P. Toporov, Effect of contact de-  
531 formations on adhesion of particles, *J. Colloid Interface Sci.* 53 (1975)  
532 314–326.
- 533 [24] C. L. Martin, R. K. Bordia, Influence of adhesion and friction on the ge-  
534 ometry of packings of spherical particles, *Phys. Rev. E* 77 (2008) 31307.
- 535 [25] D. Bouvard, R. M. McMeeking, The deformation of interparticle necks  
536 by diffusion controlled creep, *J. Am. Ceram. Soc.* 79 (1996) 666–672.

- 537 [26] O. A. Ruano, J. Wadsworth, O. D. Sherby, Deformation of fine-grained  
538 alumina by grain boundary sliding accommodated by slip, *Acta Mate-*  
539 *rialia* 51 (12) (2003) 3617–3634. doi:10.1016/S1359-6454(03)00180-0.
- 540 [27] W. M. Robertson, R. Chang, The kinetics of grain-boundary groove  
541 growth on alumina surfaces, in: W. W. Kriegel, H. Palmour (Eds.),  
542 *The Role of Grain Boundaries and Surfaces in Ceramics*, Springer US,  
543 Boston, MA, 1966, pp. 49–60.
- 544 [28] S. J. Dillon, M. P. Harmer, Intrinsic grain boundary mobility in alumina,  
545 *Journal of the American Ceramic Society* 89 (12) (2006) 3885–3887.  
546 doi:10.1111/j.1551-2916.2006.01331.x.
- 547 [29] A. Tsoga, P. Nikolopoulos, Groove Angles and Surface Mass Transport  
548 in Polycrystalline Alumina, *Journal of the American Ceramic Society*  
549 77 (4) (1994) 954–960. doi:10.1111/j.1151-2916.1994.tb07252.x.
- 550 [30] J. D. Hansen, R. P. Rusin, M. Teng, D. L. Johnson, Combined-Stage  
551 Sintering Model, *Journal of the American Ceramic Society* 75 (5) (1992)  
552 1129–1135. doi:10.1111/j.1151-2916.1992.tb05549.x.
- 553 [31] G. Gottstein, V. Sursaeva, L. S. Shvindlerman, Effect of triple junctions  
554 on grain boundary motion and grain microstructure evolution, *Interface*  
555 *Science* 7 (3) (1999) 273–283. doi:10.1023/a:1008721426104.
- 556 [32] S. G. Protasova, G. Gottstein, D. A. Molodov, V. G. Sursaeva, S. Shvin-  
557 dlerman, Triple junction motion in aluminum tricrystals, *Acta Materi-*  
558 *alia* 49 (2001) 2519–2525.

- 559 [33] X. Li, L. Zhang, Y. Dong, R. Gao, M. Qin, X. Qu, J. Li, Pressureless two-  
560 step sintering of ultrafine-grained tungsten, *Acta Materialia* 186 (2020)  
561 116–123. doi:10.1016/j.actamat.2020.01.001.
- 562 [34] Y. Dong, I. W. Chen, Mobility transition at grain boundaries in two-  
563 step sintered 8 mol yttria-stabilized zirconia, *Journal of the American*  
564 *Ceramic Society* 101 (5) (2018) 1857–1869. doi:10.1111/jace.15362.
- 565 [35] K. A. Berry, M. P. Harmer, Effect of MgO Solute on Microstructure  
566 Development in Al<sub>2</sub>O<sub>3</sub>, *Journal of the American Ceramic Society* 69 (2)  
567 (1986) 143–149. doi:10.1111/j.1151-2916.1986.tb04719.x.
- 568 [36] S. I. Bae, S. Baik, Sintering and grain growth of ultrapure alu-  
569 mina, *Journal of Materials Science* 28 (15) (1993) 4197–4204.  
570 doi:10.1007/BF00351254.
- 571 [37] S. J. Bennison, M. P. Harmer, Effect of Magnesia Solute on Surface  
572 Diffusion in Sapphire and the Role-of Magnesia in the Sintering of Alu-  
573 mina, *Journal of the American Ceramic Society* 73 (4) (1990) 833–837.  
574 doi:10.1111/j.1151-2916.1990.tb05122.x.
- 575 [38] J. Rödel, A. M. Glaeser, Anisotropy of Grain Growth in Alumina,  
576 *Journal of the American Ceramic Society* 73 (11) (1990) 3292–3301.  
577 doi:10.1111/j.1151-2916.1990.tb06452.x.
- 578 [39] J. Zhao, M. P. Harmer, Effect of Pore Distribution on Microstructure  
579 Development: III, Model Experiments, *Journal of the American Ceramic*  
580 *Society* 75 (4) (1992) 830–843. doi:10.1111/j.1151-2916.1992.tb04148.x.

- 581 [40] Z. Z. Fang, H. Wang, V. Kumar, Coarsening, densification, and grain  
582 growth during sintering of nano-sized powders—A perspective, Inter-  
583 national Journal of Refractory Metals and Hard Materials 62 (2017)  
584 110–117. doi:10.1016/j.ijrmhm.2016.09.004.  
585 URL <http://dx.doi.org/10.1016/j.ijrmhm.2016.09.004>
- 586 [41] V. Kumar, Z. Z. Fang, P. C. Fife, Phase field simulations of grain growth  
587 during sintering of two unequal-sized particles, Materials Science and  
588 Engineering A 528 (1) (2010) 254–259. doi:10.1016/j.msea.2010.08.061.
- 589 [42] R. Kawamoto, E. Andò, G. Viggiani, J. E. Andrade, Level set discrete  
590 element method for three-dimensional computations with triaxial case  
591 study, Journal of the Mechanics and Physics of Solids 91 (2016) 1–13.  
592 doi:10.1016/j.jmps.2016.02.021.  
593 URL <http://dx.doi.org/10.1016/j.jmps.2016.02.021>
- 594 [43] Z. Yan, C. L. Martin, O. Guillon, D. Bouvard, C. S. Lee, Mi-  
595 crostructure evolution during the co-sintering of Ni/BaTiO<sub>3</sub> multi-  
596 layer ceramic capacitors modeled by discrete element simulations,  
597 Journal of the European Ceramic Society 34 (13) (2014) 3167–3179.  
598 doi:10.1016/j.jeurceramsoc.2014.04.013.
- 599 [44] J. CHERMANT, M. COSTER, Granulometry and Granulomorphy by  
600 Image Analysis, Acta Stereologica 10 (1991) 7–23.  
601 URL <http://popups.ulg.ac.be/0351-580X/index.php?id=2049>
- 602 [45] Becker, J., Biebl, F., Glatt, E., Cheng, L., Grießer, A., Groß, M., Linden,  
603 S., Mosbach, D., Wagner, C., Weber, A., Westerteiger, R., Geodict Im-

604 age processing platform, GeoDict (Release 2022) [Simulation software]  
605 Math2Market GmbH, doi.org/10.30423/release.geodict2022 (2021).